

# Tectonics

## RESEARCH ARTICLE

10.1029/2019TC005637

### Key Points:

- The Nazca Ridge hosts an overthickened lower crust (10–14 km) formed in an on-ridge setting (hot spot plume near a spreading center)
- The Nazca Ridge correlates with a prominent continental slope scarp bounded by a narrow and uplifted continental shelf
- The Nazca Ridge has behaved as a seismic asperity for moderate earthquakes (e.g., 1996 *M*<sub>w</sub> 7.7 and 2011 *M*<sub>w</sub> 6.9) nucleating at depths >20 km

### Supporting Information:

- Supporting Information S1

### Correspondence to:

E. Contreras-Reyes,  
econtreras@dgf.uchile.cl

### Citation:

Contreras-Reyes, E., Muñoz-Linford, P., Cortés-Rivas, V., Bello-González, J. P., Ruiz, J. A., & Krabbenhoef, A. (2019). Structure of the collision zone between the Nazca Ridge and the Peruvian convergent margin: Geodynamic and seismotectonic implications. *Tectonics*, 38, 3416–3435. <https://doi.org/10.1029/2019TC005637>

Received 25 APR 2019


Accepted 21 AUG 2019

Accepted article online 24 AUG 2019

Published online 11 SEP 2019

©2019. American Geophysical Union.  
All Rights Reserved.

## Structure of the Collision Zone Between the Nazca Ridge and the Peruvian Convergent Margin: Geodynamic and Seismotectonic Implications

E. Contreras-Reyes<sup>1</sup> , P. Muñoz-Linford<sup>2</sup>, V. Cortés-Rivas<sup>1</sup>, J. P. Bello-González<sup>3</sup>, J. A. Ruiz<sup>1</sup>, and A. Krabbenhoef<sup>4</sup>

<sup>1</sup>Departamento de Geofísica, Facultad de Ciencias Físicas y Matemáticas, Universidad de Chile, Santiago, Chile, <sup>2</sup>Centro I-MAR, Universidad de los Lagos, Puerto Montt, Chile, <sup>3</sup>Grupo Minero Las Cenizas, Taltal, Chile, <sup>4</sup>GEOMAR-Helmholtz Centre for Ocean Research, Kiel, Germany

**Abstract** We study the structure and tectonics of the collision zone between the Nazca Ridge (NR) and the Peruvian margin constrained by seismic, gravimetric, bathymetric, and natural seismological data. The NR was formed in an on-ridge setting, and it is characterized by a smooth and broad shallow seafloor (swell) with an estimated buoyancy flux of ~7 Mg/s. The seismic results show that the NR hosts an oceanic lower crust 10–14 km thick with velocities of 7.2–7.5 km/s suggesting intrusion of magmatic material from the hot spot plume to the oceanic plate. Our results show evidence for subduction erosion in the frontal part of the margin likely enhanced by the collision of the NR. The ridge-trench collision zone correlates with the presence of a prominent normal scarp, a narrow continental slope, and (uplifted) shelf. In contrast, adjacent of the collision zone, the slope does not present a topographic scarp and the continental slope and shelf become wider and deeper. Geophysical and geodetic evidence indicate that the collision zone is characterized by low seismic coupling at the plate interface. This is consistent with vigorous subduction erosion enhanced by the subducting NR causing abrasion and increase of fluid pore pressure at the interplate contact. Furthermore, the NR has behaved as a barrier for rupture propagation of megathrust earthquakes (e.g., 1746 *M*<sub>w</sub> 8.6 and 1942 *M*<sub>w</sub> 8.1 events). In contrast, for moderate earthquakes (e.g., 1996 *M*<sub>w</sub> 7.7 and 2011 *M*<sub>w</sub> 6.9 events), the NR has behaved as a seismic asperity nucleating at depths >20 km.

### 1. Introduction

Hot spot tracks and oceanic plateaus entering a subduction zone modify the structure of the forearc system and influence dramatically the coupling degree across the subduction interface affecting both interplate and intraplate seismicity (e.g., Bilek, 2010; Contreras-Reyes & Carrizo, 2011; Wang & Bilek, 2011). In addition, the collision of oceanic high features with a convergent margin enhances subduction erosion (e.g., Balance et al., 1989; Hampel et al., 2004; Ranero & von Huene, 2000) and usually modifies locally the morphology of the upper plate causing uplift in the frontal part of the collision zone followed by subsidence as the aftermath of seamount subduction (e.g., Dominguez et al., 1998; Zeumann & Hampel, 2015).

As high oceanic features collide with the overriding plate, they will affect differently the coupling degree at the subduction interface and the upper plate deformation depending on the crustal buoyancy mode (Watts et al., 2010). For example, seamounts formed near a spreading center on weak oceanic plate (on-ridge seamounts like the Cocos and Nazca ridges) are locally more compensated and more buoyant (Watts et al., 2010), and thus, an important coupling at the subduction interface is expected. In addition, these oceanic ridges are characterized by a smooth and broad morphology (Orellana-Rovirosa & Richards, 2017) and more basal subduction erosion beneath the upper plate rather than frontal subduction erosion at the front of the upper plate is hypothesized (Contreras-Reyes & Carrizo, 2011). In contrast, oceanic ridges formed far from oceanic spreading center (off-ridge seamounts like the Juan Fernandez and Louisville ridges) are more regionally compensated, and therefore less buoyant (Watts et al., 2010), and host a rough and narrow morphology (Orellana-Rovirosa & Richards, 2017). Thus, heterogeneous and/or weaker coupling at the subduction contact (Wang & Bilek, 2011; Watts et al., 2010) and more frontal subduction erosion are expected to occur (Dominguez et al., 1998; Ranero & von Huene, 2000).

The Nazca Ridge (NR) is an on-ridge hot spot track that was formed together with the Easter Seamount Chain by the interaction between the oceanic Nazca Plate and the Easter/Sala y Gomez hot spot plume positioned near the East Pacific Rise (e.g., Ray et al., 2012). The NR is composed of abnormally thick basaltic oceanic crust, averaging  $18 \pm 3$  km thick (Hampel et al., 2004; Woods & Okal, 1994), and it has a shallow seafloor swell surface about 200–300 km wide that extends for more than 1,100 km across the oceanic Nazca Plate in the N42°E direction (Hampel, 2002). Contreras-Reyes and Carrizo (2011) estimated an anomalous normal stress of  $\sim 50$  MPa associated with the overthickened oceanic crust of the NR, which results in a considerable buoyancy force affecting the initial angle of subduction of the downgoing plate and the subduction erosion rate at the frontal part of the Peruvian convergent margin. For instance, the subduction of the NR has been correlated with a gap in arc volcanism and a subhorizontal subduction of the oceanic Nazca Plate beneath Peru (Gutscher et al., 2000; Espurt et al., 2008). In addition, Clift et al. (2003) and Stern (2011) estimated a long-term subduction erosion rate of 37–78 km<sup>3</sup>/km/Myr for the Peruvian margin. These authors, however, pointed out that subduction erosion was highly accelerated during the collision of the NR with the South American Plate with a short-term subduction rate of 115–228 km<sup>3</sup>/km/Myr.

Little seismic activity of large earthquakes ( $M_w > 8$ ) in southern Peru (14–15.5°S) has been recorded (Beck & Ruff, 1989; Villegas-Lanza et al., 2016) along the NR subduction beneath the South American Plate. For instance, there is no seismological record of any large earthquake in the ridge-trench collision zone since the historic 1868  $M_w$  8.5–9.0 megathrust earthquake (Villegas-Lanza et al., 2016). Okal et al. (2006) estimated a coseismic slip model for this event characterized by rupture south of the NR, the megathrust above the subducting NR, and at least a small segment of the interplate contact north of the NR. However, these authors used a simple rectangular fault model with uniform slip and their data are based on historic reports with large uncertainties. Nevertheless, moderate thrust events ( $M_w < 8$ ) such as the 1996  $M_w$  7.7 Nazca and 2011  $M_w$  6.9 earthquakes have been attributed to the high friction associated with the buoyant NR (e.g., Spence et al., 1999) highlighting the complex seismic pattern of this subducting oceanic ridge. The 12 November 1996  $M_w$  7.7 event broke a large zone of the shallow subduction interface of the NR, and the rupture extended for about 200-km length (e.g., Salichon et al., 2003; Spence et al., 1999). On the other hand, the 28 October 2011  $M_w$  6.9 event, a moderate thrust earthquake occurred at the northern edge of the NR with a centroid depth of 30 km according to the National Earthquake Information Center (NEIC) catalog. Apparently, the NR behaves as a barrier for earthquake rupture propagation of some large events ( $M_w > 8$ ) and as a seismic asperity for smaller events. This dual seismic behavior of the NR is intriguing and can be partially related to anomalous density zones hosted in the oceanic crust and/or upper mantle causing a heterogeneous buoyancy force transferred to the interplate boundary as the NR subducts.

In this work, we used a joint refraction and reflection traveltimes tomographic approach to derive a detailed 2-D velocity-depth model constrained by gravimetric and bathymetric data. A single seismic profile across the NR in southern Peru includes the outer rise region, trench axis, and the marine forearc (Figures 1 and 2). The profile is located near the epicentral area of the 1996  $M_w = 7.7$  and 2011  $M_w = 6.9$  earthquakes. In addition, we provide coseismic slip models for these events, which are used to discuss the role of the NR as barrier and/or asperity for earthquake rupture propagation. We present a general picture of the NR-trench collision zone and we discuss its geodynamic and seismotectonic implications.

## 2. Tectonic Setting

### 2.1. Geodynamic Setting

The Peruvian convergent margin is characterized by the subduction of the oceanic Nazca Plate beneath the continental overriding South American Plate, where geodetic observations of the Nazca-South America convergence rate predict a current azimuth of approximately N78°E direction and a convergence rate of 68–77 mm/year (DeMets et al., 1990; Norabuena et al., 1998). On the other hand, long-term paleoreconstruction models reported a convergence rate of 88–96 mm/year with an azimuth of  $\sim$ N79°E (Bello-González et al., 2018; Müller et al., 2016; Figure 3).

The age of the oceanic Nazca Plate along the Peruvian trench increases from  $\sim$ 29 Ma north of 10°S to a maximum of 51 Ma at 20°S. The oceanic plate age contrast across the Viru, Mendaña, and Nazca Fracture Zones are  $\sim$ 2,  $\sim$ 7, and  $\sim$ 4 Ma, respectively (Figures 1 and 3). The Peruvian margin strike at the NR collision zone is nearly N45°W, while the convergence vector in this area has been calculated in the range of N87°E to N76°E

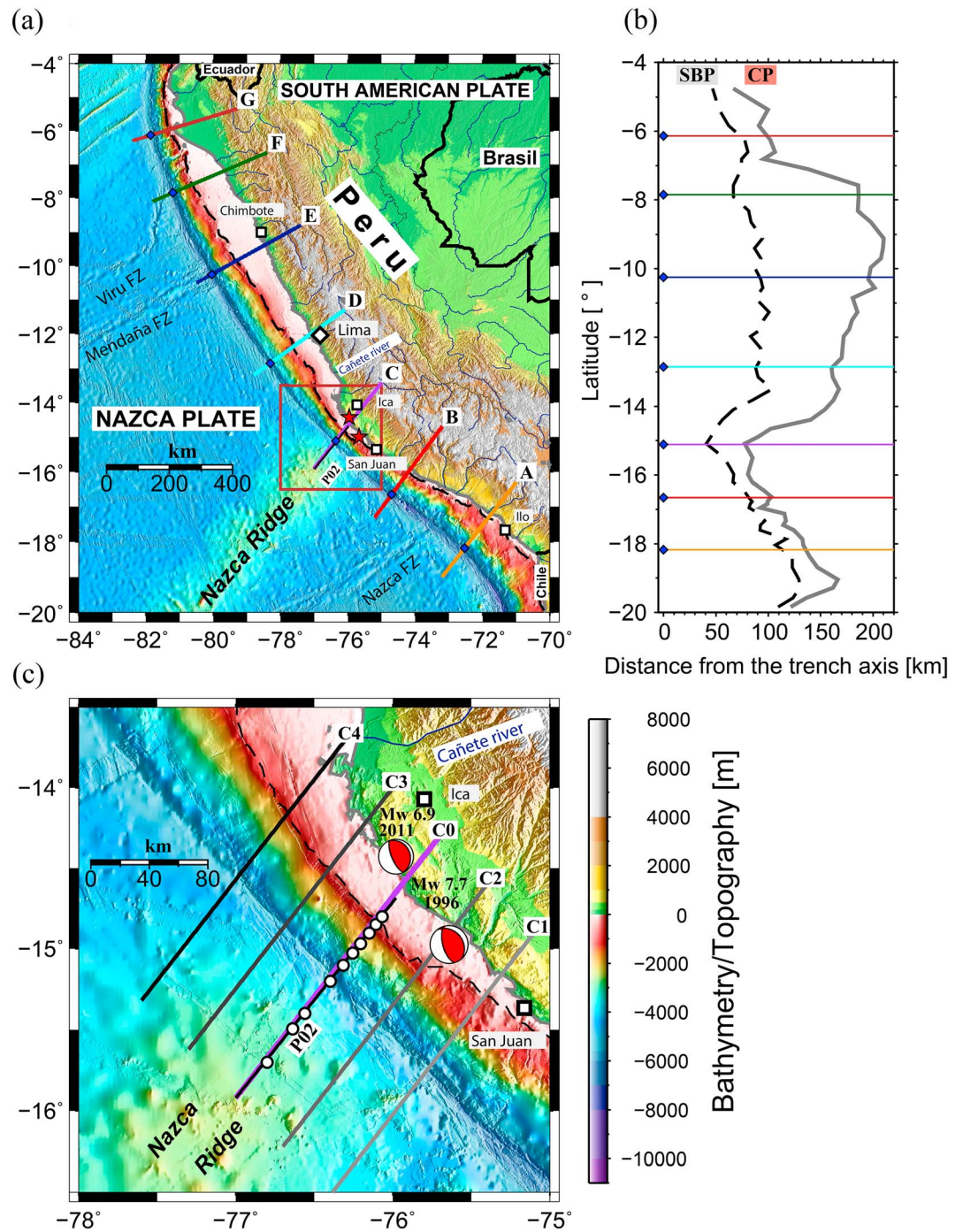


**Figure 1.** (a) Bathymetric image of the seafloor off the Peruvian convergent margin (from <https://www.gmrt.org/GMRTMapTool/>). The incoming Nazca Ridge rises some 1–2 km above the surrounding seafloor causing a local shallowing in the depth of the trench. The black dashed line corresponds to the shelf break location (topographic transition from the continental slope to the shelf). Extracted topographic profiles A–G are shown in Figure 2a. (b) Gray and dotted curves denote the perpendicular distance from the trench axis to the shelf break and coast line, respectively, shown in (a). SBP = Shelf Break Position and CP = Coast Position. (c) Solid black line (C0) is the studied wide-angle seismic profile P02, while white dots indicate the Ocean Bottom Hydrophone/Seismometers used in the traveltimes tomographic inversion. The epicenters of the 1996  $M_w$  7.7 and the 2011  $M_w$  6.9 earthquakes were calculated by the Instituto Geofísico del Perú, whereas the focal mechanism was computed by the National Earthquake Information Center. Extracted topographic profiles C0–C4 are shown in Figure 2b.

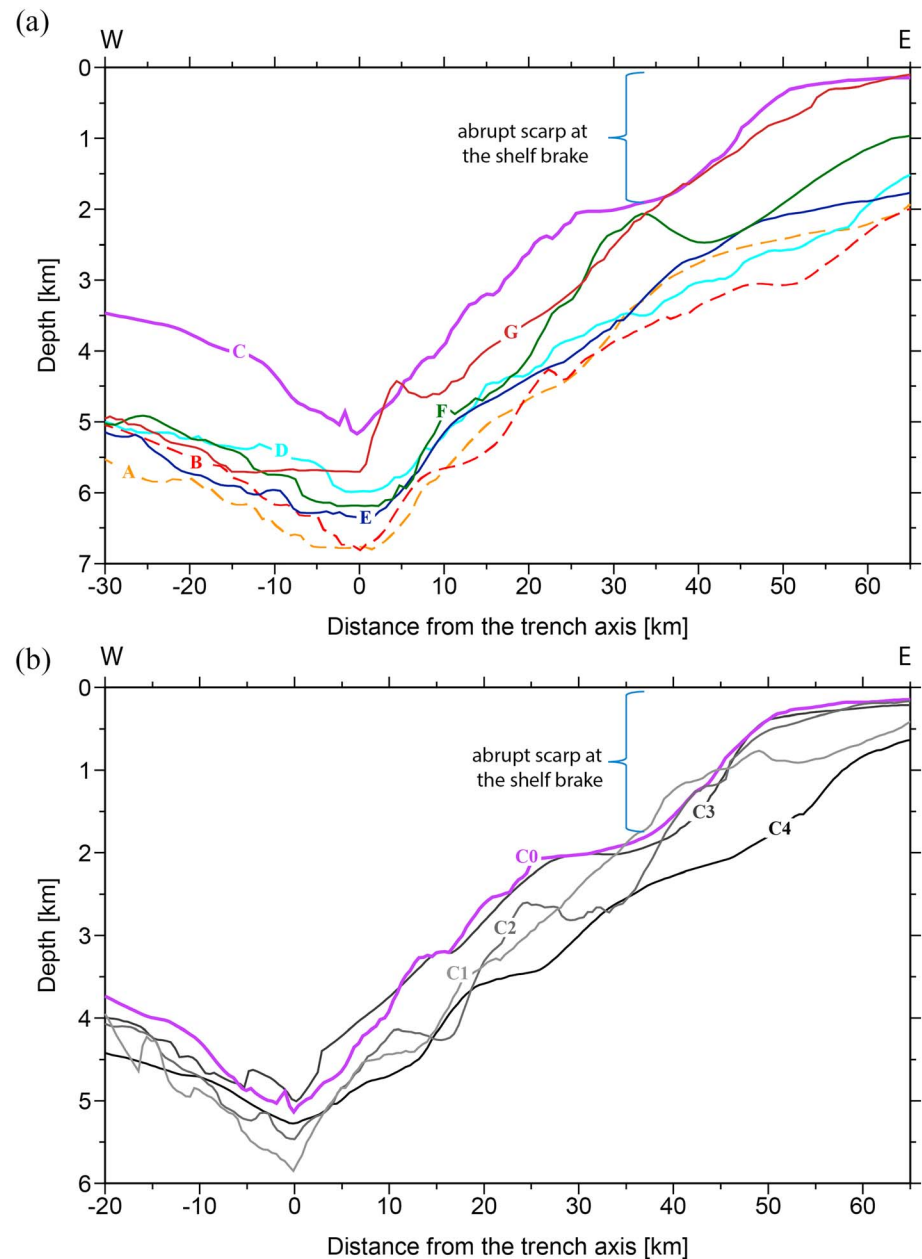


**Figure 2.** (a) Bathymetric profiles along the trench region, continental slope, and the morphological transition from the continental slope to the shelf, across the lines shown in Figure 1a. (b) Bathymetric profiles along the trench, continental slope, and continental shelf brake transition across the lines shown in Figure 1c. Please note the abrupt scarp at the shelf brake in the region of the Nazca Ridge-trench collision zone. The poorly sedimented Peruvian Trench is more than 5,500 m deep along most of the Peruvian margin, except near the ridge-trench collision zone at around 15°S where the trench shallows up to 4,500 m deep.

by Bello-González et al. (2018). Under these geometrical conditions, this setting corresponds to a sinistral regime (30–45° strike), whereas the NR collision point migrates southward along the trench at 32–60 mm/year.

The first collision of the NR with South America occurred about 40 Ma off Ecuador and since then has been migrated southward to the current collision point (Bello-González et al., 2018). Two quasi-stationary regimes of the intersection between the NR and trench took place during Neogene between 14 to 11 Ma and 5 to 3 Ma in the central Peruvian Andes at 10–12°S and 14–15°S, respectively (Bello-González et al.,

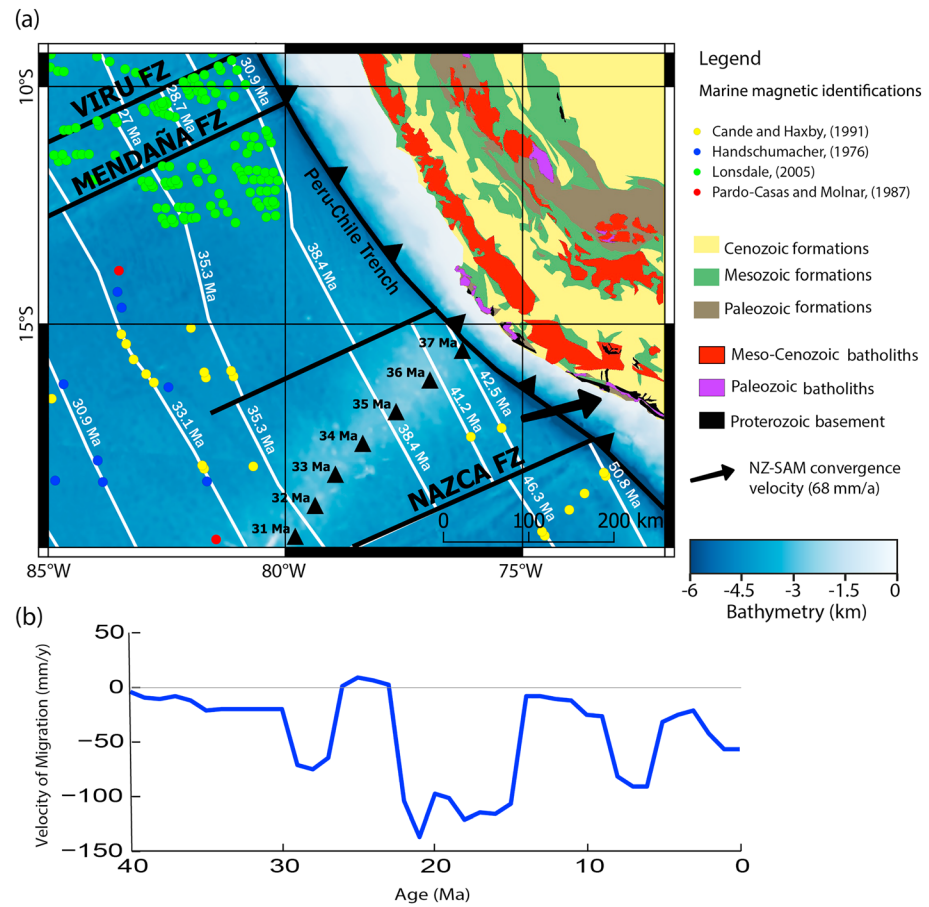


**Figure 3.** (a) Simplified geology of Peru modified from INGEMET (2016). Isochrones of the oceanic crust denoted by white curves. Black triangles represent the predicted age of the Nazca Ridge by Bello-González et al. (2018). Colored dots represent magnetic anomaly picks from the compilation of Seton et al. (2014). Source reference is shown in the legend. (b) Migration velocity of the collision point between the Nazca Ridge and the South American margin from 40 Ma to present after Bello-González et al. (2018). Positive and negative values represent northward and southward migration of the collision point, respectively.

2018). These quasi-stationary ridge subduction periods were driven by the alignment of the NR axis and the convergence velocity vector azimuth (Bello-González et al., 2018). Analog and numerical models (Espurt et al., 2008; Hsu, 1992) suggest a several million years elapse between initial positive buoyancy slab subduction and full flattening of the slab. This delay is consistent with volcanic arc activity between  $\sim 10^{\circ}\text{S}$  and  $\sim 14^{\circ}\text{S}$  until 4 Ma (Rosenbaum et al., 2005), although the NR began to enter the trench near  $\sim 10^{\circ}\text{S}$  several millions of years before (15–11 Ma; Bello-González et al., 2018; Hampel, 2002; Rosenbaum et al., 2005).

The flat slab in central Peru is considered the largest one in modern times worldwide (e.g., Antonijevic et al., 2015; Gutscher et al., 2000). Seismological studies suggest that this flat slab has a width of about 300 km and occurs at depths of 80–100 km (Ma & Clayton, 2015). Furthermore, the flat slab is located eastward of a hydrated mantle wedge and its shallowest part occurs along the subducting NR (Ma & Clayton, 2015). The cause of the flat slab is associated with a combination of factors such as trench retreat, asthenospheric suction, and subduction of a buoyant plateau decreasing the slab pull effect (Antonijevic et al., 2015; Espurt et al., 2008).

## 2.2. Regional Geological Context

The oldest seamounts of the NR prior to subduction are estimated to be 37–38 Ma (Bello-González et al., 2018). North of the NR-trench collision zone, the continental shelf is broad (50–100 km wide), whereas south and north along the ridge-trench collision zone, the shelf is narrow (<30 km wide; Figure 2). The broad

continental shelf in the north (6.5–14°S) spatially correlates with the presence of several elongated forearc basins (e.g., the Talara, Yaquina, Lima, and Pisco basins) suggesting significant Cenozoic subsidence (e.g., Kukowski et al., 2008), which was likely accelerated by the collision and southward migration of the NR along the Peruvian margin (Bello-González et al., 2018; Hampel, 2002).

Basement outcrops stretch along the Pacific coast for 800 km between the towns of Paracas and Mollendo (Figure 3). These Precambrian metamorphic rocks are hosted in San Nicolas Batolith, and extend inland for approximately 100 km. The Arequipa Massif is a continental crust fragmented whose basement is exposed along this coastal region of southern Peru and northern Chile. This massif is exposed through a series of basement outcrops spaced through the coastal region and has a magmatic and metamorphic polycyclic evolution from the Proterozoic to Mesozoic times (Ramos, 2008; Spikings et al., 2016).

After the Neo-Mesoproterozoic dispersal of Rodinia Supercontinent (Ramos, 2008), the Arequipa margin accreted to Gondwana and it had a minor rifting process and the development of a backarc basin during the Paleozoic Era but stayed together with the Amazon craton (Ramos, 2008). The Precambrian basement of the Arequipa massif has been emplaced by the Ordovician subduction-related granitoids in the coastal batholith of Peru and northern Chile (Loewy et al., 2004; Mukasa & Henry, 1990). These granitoids with arc affinities and related metamorphism are part of a larger event recognized further south like the Famatinian continental arc. This arc developed on the western margin of South America from 515 to 450 Ma (Quenardelle & Ramos, 1999). Continental rifting processes were widespread recorded in western South American margin during the Late Triassic (e.g., Charrier et al., 2007; Spikings et al., 2015). The Mitu Group petrochemical patterns were formed during continental rift along the Peruvian margin 245 to 220 Ma (Spikings et al., 2016). Later, during the first stage of subduction of the Andean cycle at 216–209 Ma is considered the Andean cycle initiation (Boekhout et al., 2013). Extension was associated with marine conditions transgression rapidly followed by the late Triassic compressional phase. This widespread extensional stage prevailed until early Cretaceous along the Andean margin (e.g., Atherton & Aguirre, 1992; Jaillard et al., 1990; Spikings et al., 2015).

### 3. Geophysical Data and Modeling

#### 3.1. Wide Angle Seismic Data and Modeling

We present wide-angle seismic data that were collected during the R/V Sonne cruise SO146-GEOPECO in 2000 along a single profile SO146-02 (P02) positioned along the NR (Figure 1). The seismic data were acquired by using ocean bottom hydrophones and three-component ocean bottom seismometers, using a total of 10 receivers covering a distance of ~197 km. The seismic source was a tuned array of three 32 l-bolt air guns that generated the seismic signal every 60 s, which corresponds to an average shot spacing of ~120 m.

Seismic profile SO146-02 (P02) was already studied by Hampel et al. (2004) using the ray tracing code of Zelt and Smith (1992). This code calculates traveltimes using asymptotic ray theory. In principle, the program allows iterative damped least squares inversion of traveltimes. This approach, however, is strongly dependent on the model parameterization. The number of layers along with the roughness of crustal interfaces makes it difficult to set up a model not biased by the parameterization. In order to reexamine the seismic structure of the seismic line P02, we present a tomographic image of the margin offshore southern Peru using the joint refraction and reflection traveltime tomography code of Korenaga et al. (2000).

We have recorded refractions through the overriding plate ( $P_{g1}$ ), reflections from the top of the oceanic crust ( $P_iP$ ) oceanic crustal refractions ( $P_{g2}$ ), Moho wide-angle reflections ( $P_mP$ ), and upper mantle refractions ( $P_n$ ) of excellent quality (see supporting information). The velocity-depth model consists of the following geological units: (1) water, (2) marine forearc basement, (3) oceanic crust, and (4) upper oceanic mantle. The seismic velocities of the continental crust of the upper plate and interplate boundary were obtained by modeling  $P_{g1}$  and  $P_iP$  phases, while the velocity structure of the oceanic crust structure was inverted using  $P_{g2}$  and  $P_mP$  phases in order to derive the velocity field and Moho depth. Finally, the velocities for the upper mantle were obtained by inverting  $P_n$  refractions. See supporting information for data examples, reference model, inversion parameters, and model resolution. The final 2-D velocity-depth model including the Derivative Weight Sum (a proxy of the ray density) is shown in Figure 4.

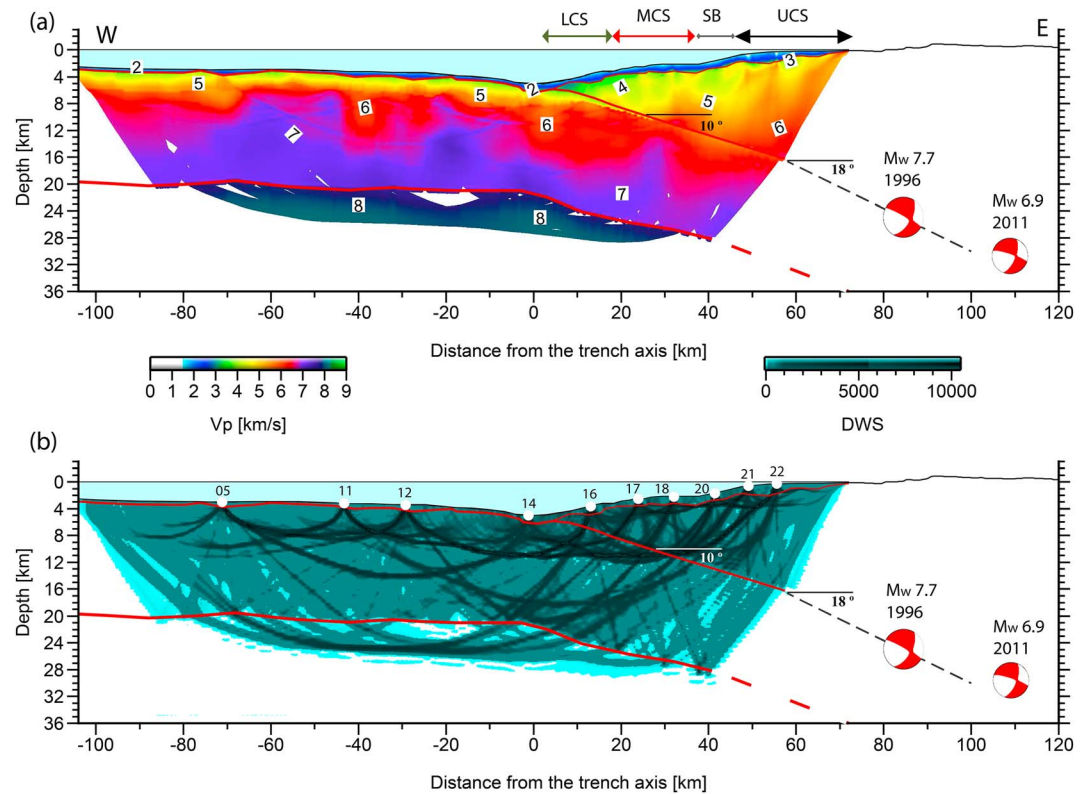


**Figure 4.** (a) Two-dimensional final velocity-depth model obtained from tomographic inversion of traveltimes along seismic line P02. Moment tensor for the 1996 and 2011 events was computed by National Earthquake Information Center. LCS = Lower Continental Slope; MCS = Middle Continental Slope; SB = Shelf Break; UCS = Upper Continental Slope. (b) DWS = Derivative Weight Sum (a proxy of the ray density).

### 3.2. Gravity Modeling

The free-air gravity anomaly data were extracted from the global gravity model of Sandwell et al. (2013) with 1-min spatial resolution. For the 2-D density-depth model, we used the code GravGrad, an interactive forward modeling approach that uses the sum of the analytical gravity responses of tabular prisms that compose layers with vertical density gradients (Maksymowicz et al., 2015). We converted the seismic velocities  $V_p$  into densities  $\rho$  using the following relationships (e.g., Maksymowicz et al., 2018): for the sedimentary section

$$\rho = 1 + 1.18(V_p - 1.5)^{0.22} \quad (1)$$

for the upper oceanic crust

$$\rho = 3.61 - \frac{6.0}{V_p} \quad (2)$$

and for the lower oceanic crust

$$\rho = 0.375(1 + V_p) \quad (3)$$

The continental crust in the ridge-trench collision zone corresponds to a fragment composed of Proterozoic and Paleozoic metamorphic and igneous rocks associated with the Arequipa Massif (Ramos, 2008, and references therein). Thus, we used the same velocity-density conversion for the oceanic and continental crust. The geometry of the subduction interface and the oceanic Moho were taken directly from the inverted 2-D velocity-depth model (Figure 4), and the landward edge of our density model is based on the hypocenter locations of the 1996 and 2011 events (Figure 4). To determine the densities below the Moho discontinuity,

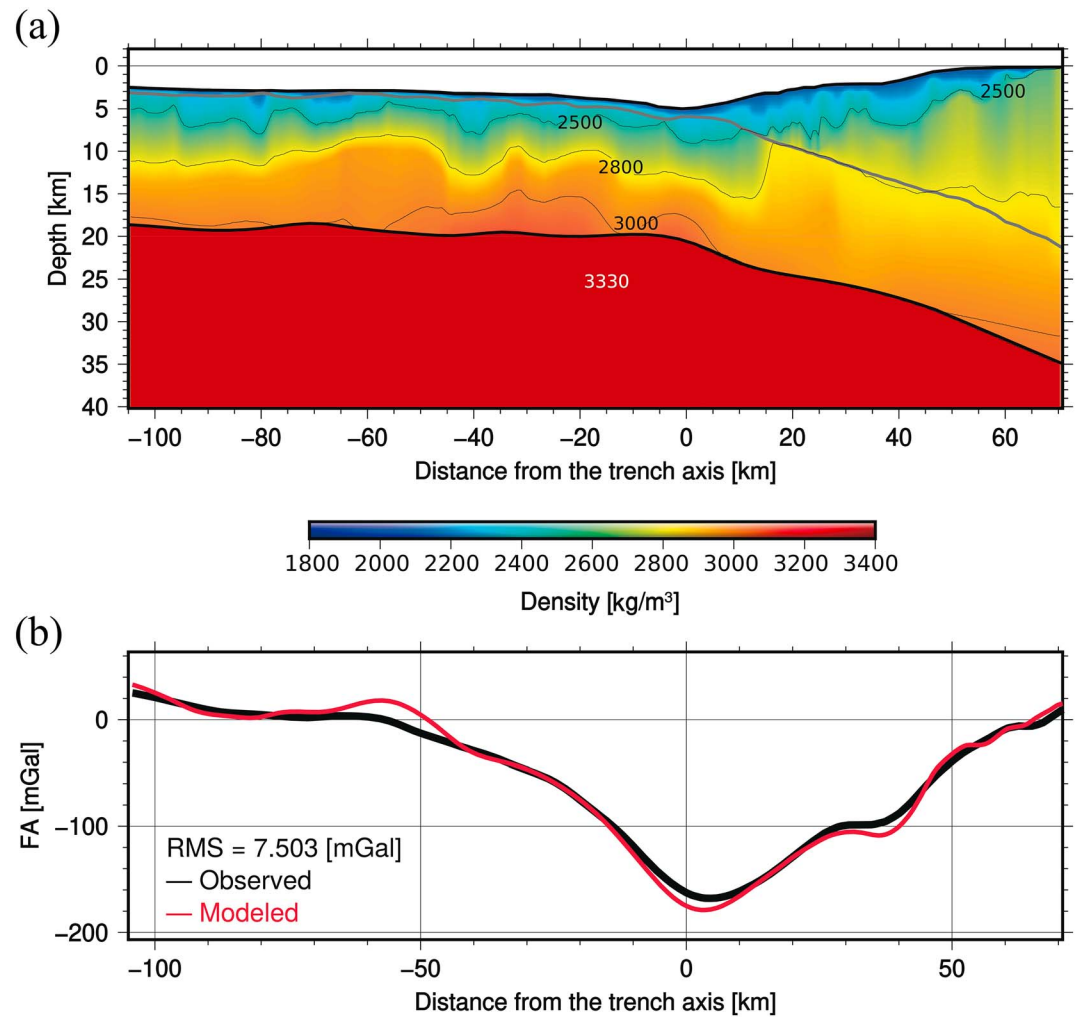


**Figure 5.** (a) Preferred 2-D density-depth model based on our 2-D velocity-depth model shown in Figure 4a. (b) The black curve is the observed gravimetric data extracted from the global gravity model of Sandwell et al. (2013). The red curve is the free air gravity anomaly calculated by using our preferred density model shown in (a).

different density-depth models were tested. We tried first a density model with a high vertical density gradient from 3,100 to 3,330 kg/m<sup>3</sup> yielding a root-mean-square misfit of about 20 mGal. Second, we tested a model including a magmatic underplating body of 5 km thickness beneath the seismic Moho characterized by a low-density zone with a vertical density gradient from 3,100 to 3,330 kg/m<sup>3</sup>. Third, we also tested a model with a mantle body with a typical constant mantle density of 3,330 kg/m<sup>3</sup>. The second and third density-depth models yield very similar RMS of ~7.6 mGal suggesting that the deeper part of the density model is largely unconstrained. We therefore choose the simplest homogenous density model with a mantle density of 3,330 kg/m<sup>3</sup> (Figure 5).

### 3.3. Seismological Constraints

In order to get some insights of source properties of the 1996 *M*<sub>w</sub> 7.7 and 2011 *M*<sub>w</sub> 6.9 earthquakes (Figures 1 and 6), we applied the finite-fault source inversion method developed by Kikuchi and Kanamori (1991). This methodology has been broadly used to invert teleseismic body waves to determine the space-time rupture history of slip. Basically, assuming a rectangular plane and a given fault geometry, the slip is estimated over a regular grid. We run several tests to determine a preferred slip model that yields the best fitting between the observed and synthetic waveforms. Broadband teleseismic waveforms were retrieved from the U. S.



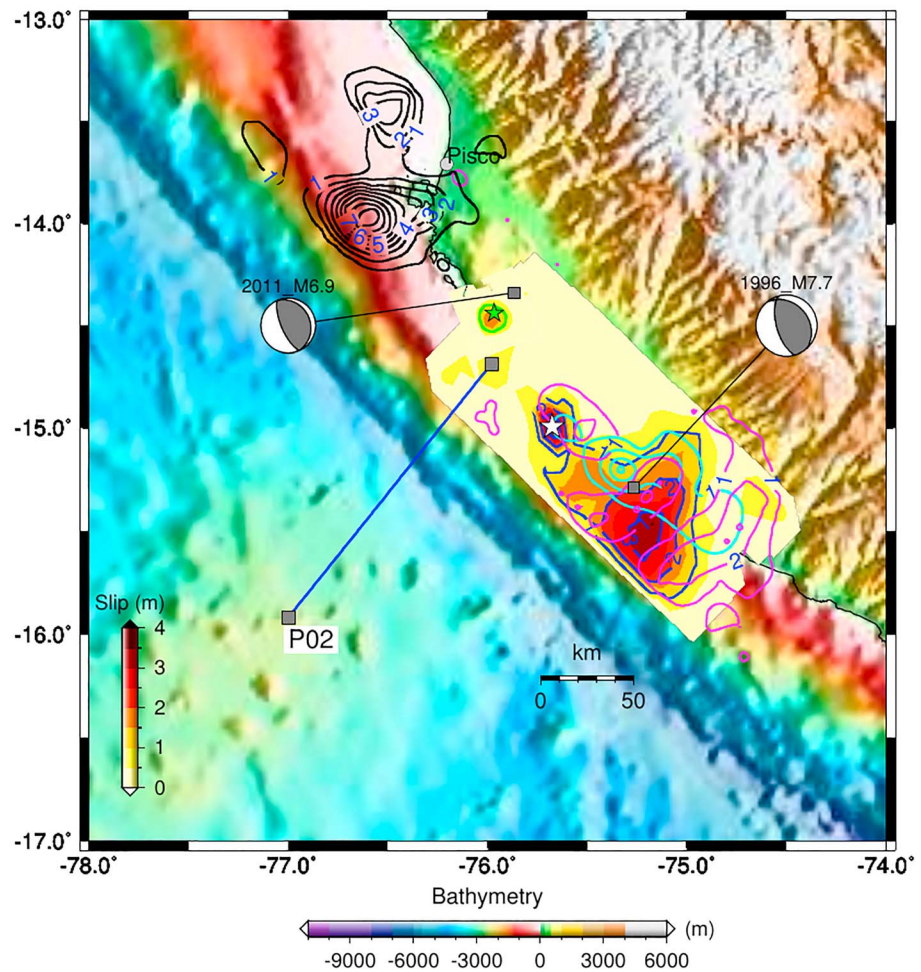


**Figure 6.** Bathymetry/topography map with slip contours at 1-m interval. The coseismic slip model for the 2007  $M_w$  8.0 Pisco earthquake (solid black lines) was downloaded from SRCMOD database (<http://equake-rc.info/SRCMOD/>; Sladen et al., 2010). Slip models computed in this study for the 2011  $M_w$  6.9 and 1996  $M_w$  7.7 earthquakes are depicted in green and blue lines, respectively, at 1-m interval. Colored stars are the epicenter location (green and white curves for the 2011 and 1996 earthquakes, respectively), and gray squares indicate centroid locations associated with the W-phase centroid moment tensor solutions from the National Earthquake Information Center. For the 1996 event, we also show the coseismic slip models of Salichon et al. (2003; cyan curve) and Spence et al. (1999; magenta curve). The location of seismic profile P02 is also indicated.

Geological Survey NEIC, for receivers located between  $30^\circ$  and  $90^\circ$  epicentral distance from the source. The instrument response is removed from the data by applying a deconvolution scheme in the time domain. The deconvolved data and synthetic seismograms are filtered in the bandpass 0.005 and 0.9 Hz prior to run the inversion. Synthetic Green's functions are computed using a 1-D crustal velocity model at the receiver and source, and for this application the velocity model proposed by Villegas and Tavera (2010) is used at the source location. Finally, we invert  $P$  waves and  $SH$  waves by selecting a time window of the respective body wave. Further details are presented in the supporting information.

#### 3.4. Integrated Geophysical Results

The top of the oceanic Nazca Plate is covered by a thin sediment sequence ( $<200$  m thick) with seismic velocities of 1.6–2.0 km/s. Likewise, the trench axis is very little sedimented (Figure 4a). The crustal structure of the NR derived from the inversion of seismic data shows a mean total crustal thickness of  $\sim 17$  km, which is about 3 times the thickness of typical oceanic Nazca crust (e.g., Grevemeyer et al., 2018). The upper oceanic crustal layer has a variable thickness of  $3 \pm 2$  km with a seismic velocity range of 4.0–6.4 km/s (Figure 4a).

The lower oceanic crust is  $12 \pm 2$  km thick with lowermost crustal velocities of up to 7.5 km/s and densities of  $3,000 \text{ kg/m}^3$  (Figures 4 and 5).

The interface between the overriding continental plate and the subducting Nazca Plate is characterized by an initial angle of subduction of  $\sim 10^\circ$  constrained by reflections from the top of the oceanic subducting crust. Deeper, the angle of subduction increases to values of  $\sim 18^\circ$  as is suggested by the location of the hypocenters of the 1996 and 2011 earthquakes. In the overriding continental plate, the velocity model shows the presence of a  $\sim 10$ -km-wide wedge-shaped body, with velocities between 2.0 and 3.0 km/s. Landward, a second unit  $\sim 50$  km wide with velocities of 4.0–5.0 km/s is bounded landward by a pronounced lateral velocity gradient from which velocities jump from values around 5.0 to  $>6.0$  km/s. This remarkably feature is fairly coincident with the prominent trenchward-dipping normal scarp observed in the bathymetric data (Figures 1 and 2).

Figure 6 summarizes the final slip models for the 1996  $M_w$  7.7 and the 2011  $M_w$  6.9 earthquakes. The rupture length of the 1996 earthquake is about 150 km, with the largest slip patch located at the southeast of its epicenter and large slip near the hypocenter. The assumed fault plane strikes  $314^\circ\text{NE}$  and dips at  $29^\circ$ ; the moment-averaged rake angle is  $59^\circ$ . The maximum slip is  $\sim 4.3$  m, and the final seismic moment is  $M_0 = 6.14 \times 10^{20}$  Nm, ( $M_w = 7.78$ ). The moment rate shows a source duration of 60 s reaching the peak at 40 s from the origin time (see supporting information). The slip of the 2011  $M_w$  6.9 event is distributed over a  $20 \times 20$ -km<sup>2</sup> area and shows a peak slip of 1.95 m. The fault geometry was set with a dip of  $20^\circ$  and strike of  $338^\circ$ , whereas the moment-averaged rake angle is  $79^\circ$ . The solution yields a seismic moment of  $M_0 = 2.39 \times 10^{19}$  Nm ( $M_w = 6.85$ ). The moment rate reaches its maximum value at  $\sim 6$  s after the initiation of the rupture and shows a source duration of about 15 s (see supporting information).

## 4. Interpretation and Discussion

### 4.1. Oceanic Crust and Mantle beneath the NR

Velocities in the  $3 \pm 1$ -km-thick upper crust layer are between 3.5–4.0 km/s at the top and 6.0–6.2 km/s at the bottom interpreted as a sequence of extrusive basalts on top of a sheeted dike complex. About 55 km westward of the trench axis, the velocity model shows the presence of relatively high shallow upper crustal layer, which is coincident with the location of a small seamount seen in the bathymetric map (Figures 1 and 2) and also mapped by seismic reflection data (Hampel et al., 2004). This seamount outcrops from the sediment bed ponded on top of the Nazca plate (Hampel et al., 2004).

The NR presents a very thick lower crust of  $12 \pm 2$  km thickness composed likely of gabbroic rocks and the possible presence of intrusions in the lowermost crust with seismic velocities falling in the range of 6.7–7.5 km/s (Figure 4). Overthickened lower crusts have also been observed across the Cocos and Carnegie Ridges at the northern boundary of the Nazca Plate (Sallares et al., 2003), both formed at the Galapagos hot spot on effectively zero-age lithosphere at an active spreading center (the East Pacific Rise). We therefore concluded that the interaction between the East Pacific Rise and the hot spot plume (Easter/Sala y Gomez Hot spot) promotes the overthickening of the gabbroic crust and the magmatic intrusion into the base of the oceanic crust as has been pointed out by the seismic compilation of Richards et al. (2013).

The overthickened crust represents an anomalously body with a density similar to gabbro ( $3,000$ – $3,100 \text{ kg/m}^3$ ) but lower than the surrounding mantle peridotite ( $3,330 \text{ kg/m}^3$ ). This anomalous density contrast causes strong buoyancy forces and subsequently the formation of the broad swell (shallow seafloor) topography (McNutt & Bonneville, 2000; see detailed discussion of the swell topography in the next subsection). For the case of the NR, the swell surface is up to 1.5 km shallower than the surrounding seafloor (Figures 1 and 2) and is characterized by a smooth morphology compared to other hot spot tracks formed by hot spot plumes located far from active spreading centers such as the Juan Fernandez Ridge and the Hawaiian volcanic chain (e.g., Orellana-Rovirosa & Richards, 2017). According to these authors, the smooth swell topography occurs when the hot spot plume is overlying by an oceanic lithosphere young, and therefore weak, thin, and hot, allowing voluminous melt penetration and crustal intrusion. This hypothesis is consistent with the geodynamic setting of the young oceanic Nazca Plate and the location of the Easter/Sala y Gómez hot spot sited near the active East Pacific spreading center.

Upper mantle velocities are in the range of 7.8–8.2 km/s, whose lower bound is lower than normal mantle peridotite (e.g., Grevemeyer et al., 2018). The reduced upper mantle velocities can be explained by mantle

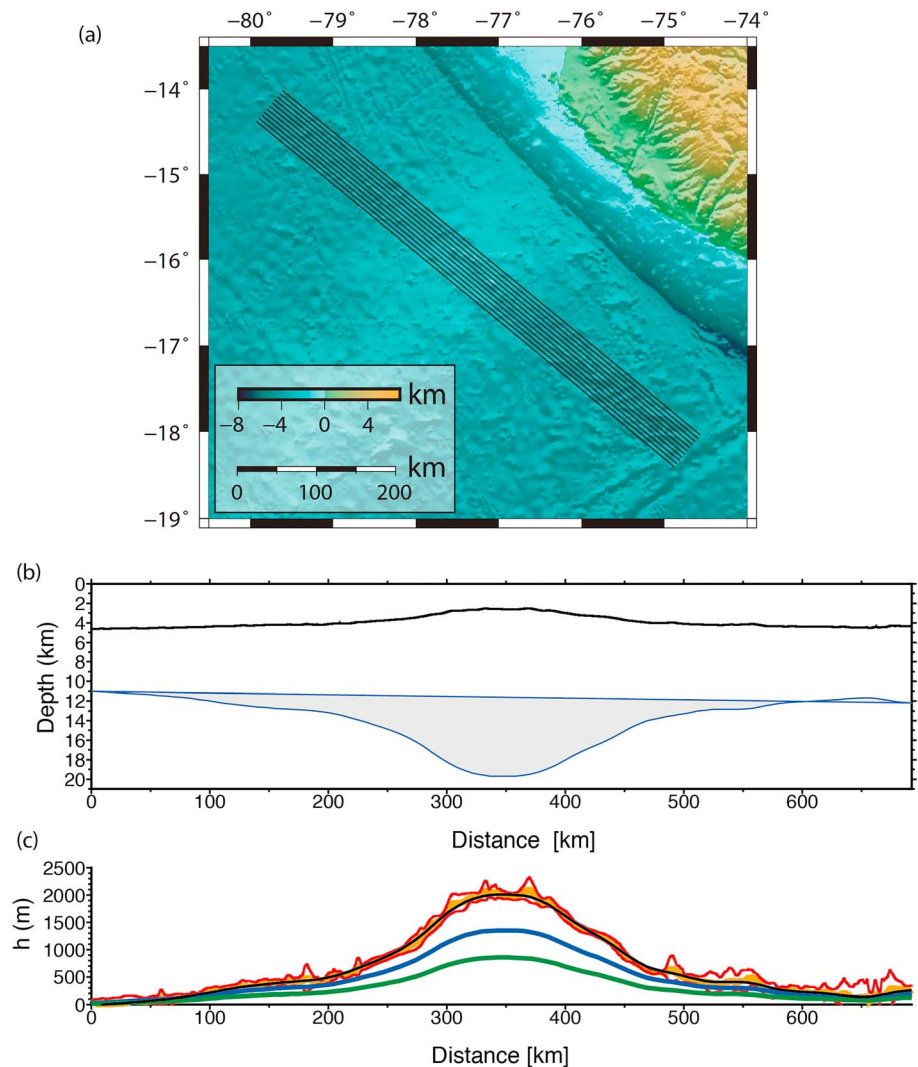


**Figure 7.** (a) Location of the 10 bathymetric profiles that were extracted and stacked to form an averaged section shown in (c). (b) The Moho depth location beneath the Nazca Ridge was taken from the seismic results of Hampel et al. (2004) and the gravimetric models of Cortés-Rivas et al. (2018). (c) The orange curve represents the stacked and averaged bathymetry. This curve was filtered using a median filter with a 2-km moving window (black curve). The blue curve corresponds to the isostatic response  $h_s(x)$  by using a lower crust density of  $\rho_{lc} = 3,000 \text{ kg/m}^3$ . The green curve denotes the thermal swell signal, which corresponds to the filtered bathymetric profile minus the  $h_s(x)$ .

hydration (serpentinization) trough extensional bend faults or by the presence of magmatic material from the hot spot plume ponded beneath the Moho (Kopp et al., 2004). However, the gravimetric model does not display considerably reduced mantle densities, so we rule out the possibility of large magmatic material ponded beneath the Moho or deep mantle hydration (also suggested by seismological studies in the study region by Kumar et al. (2016)). Instead, the velocities of 7.0–7.5 km/s in the lower crust and the overthickened crust suggest that magmatic materials are intruded into the oceanic crust rather than ponded beneath the Moho.

#### 4.2. Swell Topography of the Nazca Ridge

The Nazca Ridge is surrounded by a smooth and broad region of shallow seafloor (swell topography). To characterize the amplitude and wavelength of this uplifted surface, we extracted ten bathymetric profiles sited SW of the Peruvian Trench (Figure 7a) in order to avoid the topography effect of the outer rise caused by the bending of the plate prior to subduction. The extracted bathymetric profiles are spaced at an interval

of 5 km and were stacked together to form a single section from which the average bathymetric profile and the standard deviation were computed. We also filtered the average bathymetric profile using a median filter (2 km moving window) to reduce the high-frequency noise (Figure 7b). The swell topography has a maximum amplitude of ~2,000 m high, an average amplitude of ~965 m, and a wavelength of 600–700 km wide.

The swell topography is associated with buoyant forces from below causing the uplift of the seafloor, and its origin is usually caused by a combination of thermal and chemical processes. The thermal effect is linked to the dynamic surface uplift from the rising mantle plume (e.g., Phipps Morgan & Morgan, 1995), while the chemical effect is due to the magmatic underplating beneath the Moho or crustal thickening that renders rocks less dense than the surrounding unaltered upper mantle (McNutt & Bonneville, 2000).

For the NR case, the chemical effect should be caused mainly by the anomalous crustal thickness ~17 km (Figure 4) versus the normal oceanic crustal thickness of ~6 km according to the seismic results obtained from wide-angle seismic lines located at ~100, ~200, and ~300 km north of the NR (Krabbenhoft et al., 2004). The uplift surface caused by the anomalous crustal thickness can be modeled as a buoyant load flexing the elastic plate up from below (e.g., McNutt & Bonneville, 2000). In the wavenumber domain the uplift surface  $\tilde{H}_s(k)$  caused by the loading of an elastic plate from beneath by a load  $\tilde{U}(k)$  is given by (e.g., Watts, 2001)

$$\tilde{H}_s(k) = \tilde{U}(k) \frac{(\rho_m - \rho_u)}{(\rho_u - \rho_w)} \left[ 1 + \frac{Dk^4}{g(\rho_m - \rho_w)} \right]^{-1} \quad (4)$$

where  $\rho_u$ ,  $\rho_w$ , and  $\rho_m$  are the densities of the underplating load, water, and mantle, respectively.  $D$  is the flexural rigidity (a proxy of the stiffness of the elastic plate),  $k$  is the spatial wavenumber, and  $g$  is the acceleration of gravity (e.g., McNutt & Bonneville, 2000; Watts, 2001).

Because the Easter hot spot plume is located near an active spreading center (East Pacific Rise), the NR was formed on a zero-age plate setting, and therefore, the oceanic plate at the time of volcano emplacement had little flexural rigidity (e.g., Calmant et al., 1990). Thus, we can assume local isostasy, which means  $D \rightarrow 0$ , and the equation reduces to in the spatial domain

$$h_s(x) = u(x) \frac{(\rho_m - \rho_u)}{(\rho_u - \rho_w)} \quad (5)$$

The value for  $u(x)$  is set to  $u(x) = m(x) - h_c$ , where  $m(x)$  defines the seismic Moho geometry, which is taken from the seismic results of a processed seismic line sited perpendicular to the NR axis (Hampel et al., 2004) and complemented by a gravimetric model of Cortés-Rivas et al. (2018).  $h_c = 6$  km is the “normal” oceanic crustal thickness north of the NR according to the 2-D velocity-depth models of Krabbenhoft et al. (2004).  $h_s(x)$  is computed using  $\rho_u = 3,000 \text{ kg/m}^3$  for the lower overthickened crust. This value is taken from the 2-D density-depth model shown in Figure 5. The results show that the isostatic response explains the ~70% of the uplifted surface, whereas the remaining swell surface is induced by the thermal effect of the elevated temperature of the underling asthenosphere (Figure 7).

The mass anomaly with the swell topography can be represented by the buoyancy flux  $B_f$ , which quantifies the rate of hot spot swell formation (e.g., Adam et al., 2005). It can be assumed that the excess mass associated with the swell is compensated by the mass deficit of the hot (less dense) plume rock impinging on the base of the oceanic lithosphere (e.g., Sleep, 1990; Turcotte & Schubert, 2014). Thus,  $B_f$  can be estimated using

$$B_f = (\rho_m - \rho_w)wEV_L \quad (6)$$

where  $\rho_m - \rho_w = 2,330 \text{ kg/m}^3$  is the mantle/water density contrast,  $w$  is the swell’s width,  $E$  is the mean amplitude of the swell, and  $V_L$  is the plate velocity (Sleep, 1990). Note that  $wE$  is the cross-sectional area of the swell in a vertical cross section perpendicular to the hot spot track axis.

The age of the NR swell prior to subduction is about 37 Ma (Bello-González et al., 2018), and it was formed on the former Nazca plate (the Farallon Plate; e.g., Müller et al., 2016). Considering the Easter hot spot motion predictions (Bello-González et al., 2018; Doubrovine et al., 2012) and tectonic reconstruction

models (Bello-González et al., 2018; Müller et al., 2016), the predicted Farallon plate velocity relative to the Easter Hot spot is  $\sim 100$  mm/year (Bello-González et al., 2018; Doubrovine et al., 2012; Müller et al., 2016). So, we use  $V_L = 100$  mm/year in equation (6). From Figure 7, we take  $w = 500$  km and the calculated mean thermal swell amplitude  $E$  is about 200 m (both estimated values refer to the swell caused by the thermal contribution). Thus, we find  $B_f \sim 7.4$  Mg/s.

This value is similar to the estimated buoyancy flux for Hawaii ( $\sim 7$  Mg/s) by Turcotte and Schubert (2014) or higher ( $4 \pm 0.7$  Mg/s) than the  $B_f$  reported by Adam et al. (2005). For the same Nazca plate, Turcotte and Schubert (2014) reported a buoyancy flux of about 1.4 Mg/s for the Juan Fernandez Ridge whose hot spot is located approximately 900 km offshore central Chile. Thus, our estimated relatively high  $B_f$  value for the NR (constrained by seismic and gravimetric data) reflects the high thermal anomaly associated with the combined effect of the Easter/Sala y Gomez hot spot plume and the active spreading center of the East Pacific Rise.

Regardless of the origin for the swell topography (thermal and/or chemical), the total buoyant effect caused by both the thermal reheating of the lithosphere and the anomalous crustal thickness results in the pronounced swell morphology causing anomalous normal stress at the interplate contact. This process directly affects the mechanisms of subduction erosion and the frictional behavior of the interplate contact. These two processes are further discussed in sections 4.3 and 4.4, respectively.

### 4.3. Subduction Erosion of the Continental South American Plate Caused by the Collision of the NR

The frontal part of the margin is characterized by a poorly sedimented trench as a consequence of little sediment supplies from the Andes to the trench offshore the arid desert along the coastal area of southern-central Peru (e.g., Troll, 1968). In addition, the high relief topography in the ridge-trench collision zone has caused the debris deposition to be preferentially transported toward deeper topography of the trench (northward and southward of the NR axis). In this area, the continental slope is relatively steep ( $\sim 18^\circ$ ), while the toe of the margin has a small frontal prism with seismic velocities of 1.7–2.5 km/s (Figure 4a). Between the middle continental slope and the shelf break at 10–50 km landward of the trench axis (Figure 4), the slope apron is composed of Paleogene and Neogene slope deposits dominated by extensional structures (Romero et al., 2013). Further north, in the Lima forearc basin, von Huene et al. (1996) have identified back-thrust structures, which were attributed as evidence for the contraction caused by the NR collision (Romero et al., 2013).

Beneath the continental slope, seismic velocities increase from 3.5 to  $\sim 5.0$  km/s and are interpreted as the metamorphic and igneous Arequipa massif basement that forms part of the outermost forearc block (Figures 3 and 4). Likely, this unit is characterized by a significant degree of rock deformation, since the outermost forearc block is sited at shallow lithostatic pressures where failure requires low deviatoric stresses and therefore subduction erosion is more intense (Contreras-Reyes et al., 2014).

Based on (1) the observed seismic velocities of  $6.0 \pm 0.4$  km/s landward of the shelf break, (2) the spatial distribution of basement outcrops (Figure 3), and (3) the geological map of the offshore continental basement provided by Romero et al. (2013), we interpret that the continental crust of the central Peruvian margin in the coastal region is associated with the Proterozoic to Mesozoic batholiths and metamorphic units of the Arequipa Massif. The continental slope-shelf transition is highlighted by a pronounced normal trench-dipping scarp of  $\sim 1.5$  km high (Figures 1 and 2). This abrupt morphological change overlies a high lateral velocity gradient at 20–40 km from the trench axis, from which velocities increase landward from 5.0 to  $>6.0$  km/s suggesting that vigorous subduction erosion has ceased and/or the igneous framework is not very fractured or hydrated. Similar features have been observed along the erosive northern Chilean margin at 31–22°S (Contreras-Reyes et al., 2012, 2014; Maksymowicz et al., 2018).

The collision of the “buoyant” NR with the South American continental plate enhances subduction erosion and shallows the trench locally. North of the ridge-trench collision zone, the trench is up to 2 km deeper (Figures 1 and 2) suggesting long-term subsidence of the outermost forearc block caused by long-term subduction erosion and accelerated by short-term basal subduction erosion caused by the NR (e.g., Hampel et al., 2004). Moreover, diverse geomorphology sedimentology, low-temperature thermochronology, and surface isotopic studies on the coastal area at 15°S where the NR has been subducting since Late Miocene

reveals coeval surface uplift events (Hsu, 1992; Le Roux et al., 2000; Saillard et al., 2011; Wipf et al., 2008). Furthermore, Bourgois et al. (1988) suggest that the middle continental slope off Peru is undergoing tension and massive collapse, while the frontal prism accumulated a large amount of debris produced by this mass wasting events.

A striking morphological feature of the NR collision is the narrow continental slope in the ridge-trench collision zone (40–50 km wide). In contrast, adjacent to the collision zone, the slope becomes at least twice as wide and the coastal line migrates seaward (Figure 2) reflecting high uplift rates associated with the strong buoyancy forces of the NR. The collision zone is also highlighted by the presence of a normal trenchward-dipping scarp located in the transition from the slope to the shelf (Figure 2). The normal scarp, however, is absent to the north and south of the ridge-trench collision zone suggesting low subsidence and uplift rates seaward and landward of the shelf break, respectively, in comparison with the ridge-trench collision zone.

As we pointed out, the swell topography of the NR is smooth compared to other hot spot tracks such as the Juan Fernandez and Louisville ridges formed onto old oceanic lithosphere far from the spreading center. These oceanic ridges might have the potential to erode basally the upper plate during their subduction causing a tunnel abrasion effect and subsequent subsidence of the continental crust. Furthermore, some authors speculate about the decapitation process at larger depths (Cloos & Shreve, 1996). In the case of the NR, the smooth swell topography should have a lower abrasion tunneling effect, but its large buoyancy force would increase the anomalously high normal stress causing primarily high friction and basal subduction erosion followed by hydrofracturing and hence a decrease of the interseismic coupling (e.g., Le Pichon et al., 1993; Wang & Bilek, 2011). In addition, seismological studies reported high  $V_p/V_s$  ratios at seismogenic depths as well as in the flat slab region and has been attributed to the presence of a fluid-rich layer (Kim & Clayton, 2015). This low strength material might be associated with the eroded material from the overriding plate due to the collision of the NR and is transported at larger depths.

#### 4.4. Seismotectonic Implications

Historical reports over the last five centuries suggest that the last megathrust earthquake with estimated  $M_w$  of 8.5–9.0 occurred in 1746 just northwest of the subducting NR (the so-called Lima-Callao earthquake; Dorbath et al., 1990). In addition, the NR has mainly behaved historically as a barrier for along-strike rupture propagation of megathrust earthquakes ( $M_w \geq 8$ ) such as the 1942  $M_w$  8.1, 1974  $M_w$  8.0, and 2007  $M_w$  8.0 events (e.g., Okal & Newman, 2001; Sennson & Beck, 1996; Sladen et al., 2010; Villegas-Lanza et al., 2016). In the particular case of the relatively recent Pisco 2007  $M_w$  8.0 event, Bilek (2010) used teleseismic data and obtained a slip model where some slip concentrated at the northern flank and above of the subducting NR (Figure 8). On the other hand, Sladen et al. (2010) used a joint data set combining teleseismic body waves, Interferometry Synthetic Aperture Radar, tsunami waveforms, and field observations to invert a refined coseismic slip model. Their results show two patches of slip concentrated at the northern flank of the subducting NR (Figure 8), and thus, for this event the subducting ridge behaved apparently as a barrier arresting southward rupture propagation.

According to the results of geodetic campaigns conducted between 2008 and 2013 along the Peruvian margin, the interplate contact in the ridge-trench collision zone is practically decoupled in the interseismic period, whereas the NW and SE bounds of the NR are highlighted by two strongly locked zones (Villegas-Lanza et al., 2016). This seismic behavior is antiintuitive owing to the smooth and uplifted seafloor of the buoyant NR that causes increased normal stresses at the subduction interface. However, the anomalous normal stress also triggers subduction erosion at the base of the overriding plate and subsequently a weaker seismic coupling (e.g., Contreras-Reyes & Carrizo, 2011; Wang & Bilek, 2011). Thus, the creeping behavior at the fault zone is consistent with an interplate contact highly eroded and hydrofractured causing the reduction of friction and coupling enhanced by the subduction of the NR. Furthermore, several studies have concluded that most of the events of the 20th and 21st centuries broke in the deeper part of the seismogenic zone along the southern and central Peruvian margin (Norabuena et al., 1998; Spence et al., 1999). This suggests that the stress absorption is inelastically in the shallow part of the megathrust fault zone where subduction erosion is more efficient due to the low lithostatic pressures. In contrast, at larger depths (>20 km) subduction erosion is weaker and stick-slip behavior along the thrust fault zone can occur.

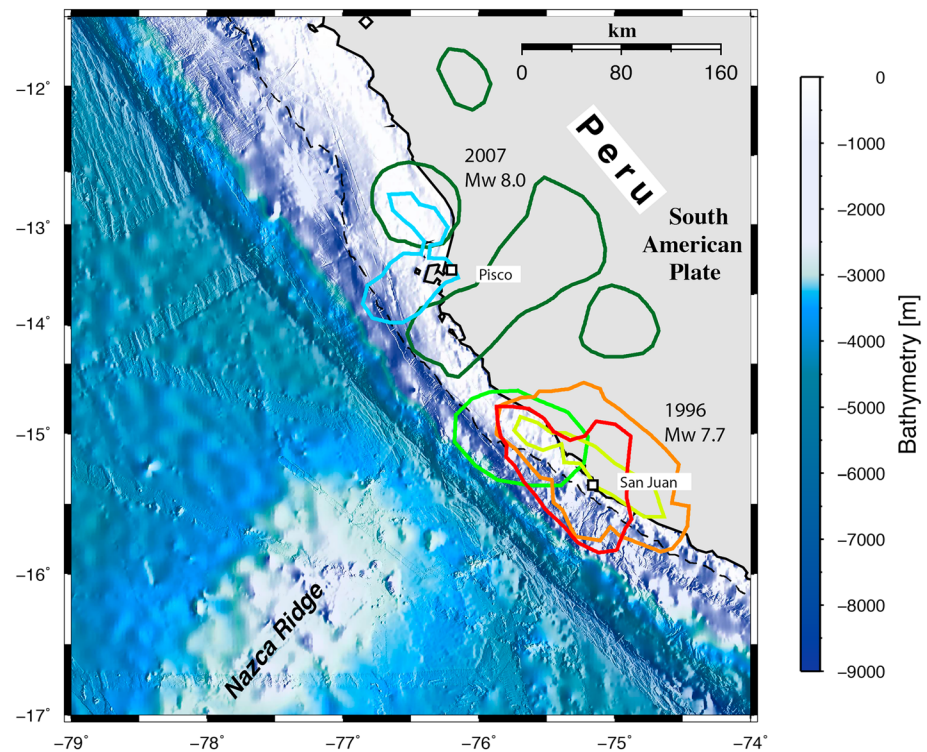


**Figure 8.** (a) The dark green curves correspond to the earthquake rupture area of the 2007  $M_w$  8.0 Pischo earthquake based on the coseismic fault slip model of Bilek (2010). Fault slip model after Sladen et al. (2010) for the same event (light blue curve) is also shown for comparison. For the 1996  $M_w$  7.7 Nazca event, the orange and yellow curves represent the rupture areas of Spence et al. (1999) and Salichon et al. (2003), respectively. For the same event, the red curve denotes our model shown in Figure 6, whereas the light green curve depicts the coseismic slip model of Bilek (2010).

Wang and Bilek (2011) argued that the process of seamount subduction develops a complex fracture network facilitating the generation of small earthquakes and aseismic creep rather than the generation of large earthquakes. The heterogeneous morphology of subducting seamounts should cause large resistance (mainly aseismic) causing pervasive local deformation, and not affecting the large-scale strength of a frictional contact, that governs the seismogenic behavior of the interplate fault zone (Wang & Bilek, 2011). This behavior has also been observed in ridge-trench collision zones of seamounts with rough topography such as the Juan Fernandez Ridge off central Chile or the Cocos Ridge off the Osa Peninsula in Costa Rica (Tajima & Kikuchi, 1995; Ruiz et al., 2018; Van Rijnsingen et al., 2018). The NR presents a similar seismic behavior despite its smooth adjacent topography suggesting that the buoyancy forces should have a complex pattern in transferring the anomalous normal stresses to the interplate fault zone causing creeping behavior and stick-slip behavior at short scales.

Figures 4 and 6 show that the 1996  $M_w = 7.7$  and 2011  $M_w = 6.9$  thrust earthquakes are located beneath the continental shelf in the coastal region at depths in the range of 25–30 km. These relatively large events suggest that for larger depths (beneath the Arequipa Massif) the aseismic/creeping behavior discussed above is no longer valid, and the lithostatic pressures of the overriding rocks affect the tectonic erosive mode of the interplate contact and upper plate. In fact, several seismic studies carried out in erosive margins suggested the cessation of hydrofracturing, porosity, and subduction erosion at depths  $>20$  km by the increase of seismic velocities (e.g., Contreras-Reyes et al., 2014; Sallares & Ranero, 2005). Our seismic results for the NR reveal that subduction erosion is more vigorous beneath the continental slope facilitating abrasion and hydrofracturing and hence an aseismic behavior. Landward of the shelf break, the seismic behavior of the interplate contact is reflected by the occurrence of earthquakes with magnitudes up to  $M_w$  7.7 in an environment with upper plate rocks with relatively high bulk densities beneath the continental shelf (Figures 4 and 5). In this region, uplift of the coastal block continues to be active causing the formation of the Peninsula de Paracas belonging to the Arequipa Massif (Figure 3).

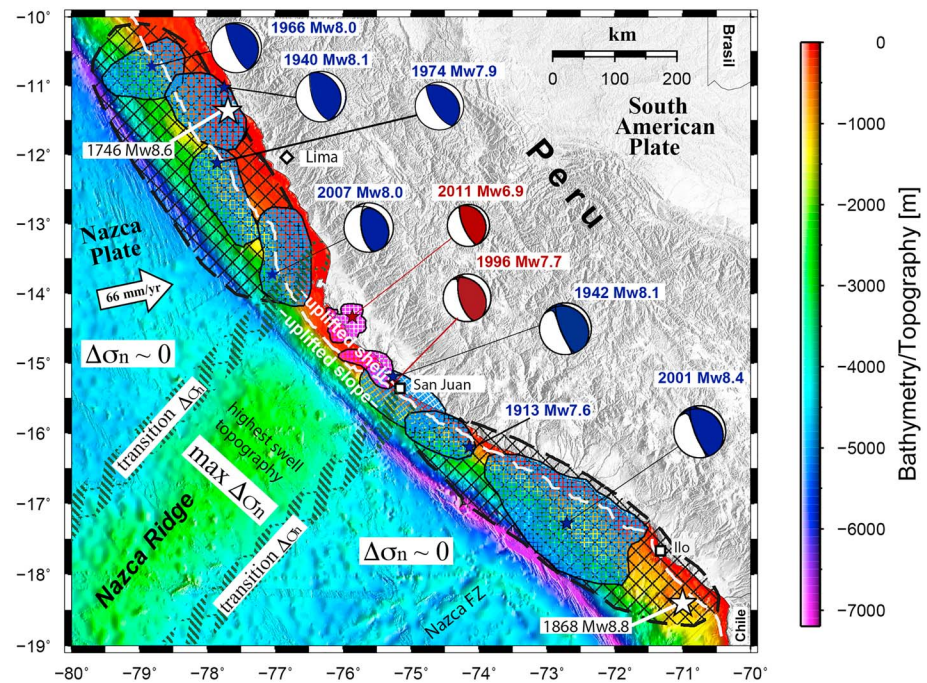


**Figure 9.** The shallow topography (swell) associated with the buoyancy forces of the Nazca Ridge has a maximum amplitude of 2,000 m at the middle of the axis of the ridge. The swell region is characterized by anomalously high normal stress  $\Delta\sigma_n$  associated with the anomalously thick oceanic crust with estimated maximum values of  $\sim 50$  MPa (Contreras-Reyes & Carrizo, 2011).  $\Delta\sigma_n$  decreases progressively to the edges of the swell topography (illustrated by the shared zones) up to the regions of steady normal stress associated to normal oceanic crust  $\sim 6$  km thick (Kranbenhoef et al., 2004). The white dashed line denotes the position of the shelf break (transition from the continental slope to the shelf). The collision zone is characterized by high uplift rates of the trench, continental slope, and shelf associated to the strong buoyancy forces of the Nazca Ridge. Subduction erosion is more efficient beneath the continental slope at low lithostatic pressures causing hydrofracturing and creeping aseismic behavior. The 1996 and 2011 thrust earthquakes located beneath the shelf in the coastal region underlying by an interplate contact where subduction erosion is less intense and stick-slip behavior can occur. The earthquake rupture areas are taken from Villegas-Lanza et al. (2016). Please note the close location for the epicenters of the 1942 and 1996 events at the southern flank of the Nazca Ridge. The rupture front propagates predominantly southward to regions where  $\Delta\sigma_n$  vanishes.

Figure 9 summarizes our interpretation for the seismic behavior of the NR. The strong buoyancy forces associated with the anomalously thick underlying oceanic crust cause anomalous normal stress and uplift and vigorous subduction erosion predominantly beneath the continental slope. Subduction erosion in the form of hydrofracturing at the base of the upper plate causes creeping (weak coupling) in the ridge-trench collision zone, which behaves as a barrier for large earthquakes. Beneath the continental shelf, subduction erosion is less intense and hydrofracturing degree of the upper plate decreases. Thus, small to moderate earthquakes can nucleate but their size is limited by the frictional heterogeneities of the plate contact.

## 5. Conclusions

From our derived 2-D velocity and density models, coseismic slip models for 1996 *Mw* 7.7 and 2011 *Mw* 6.9 earthquakes, and morphological analysis in the collision zone between the NR and the South American Plate we drawn the following conclusions:

1. The NR has a lower crust intruded by large volumes of gabbroic (mafic) rocks ( $V_p \sim 6.8\text{--}7.5$  km/s and densities of  $2,800\text{--}3,000$  kg/m<sup>3</sup>). The total thickness of the oceanic crust is  $\sim 17$  km, and there is no clear evidence for the presence of magmatic material beneath the oceanic Moho.
2. The NR is characterized by an adjacent smooth shallow seafloor (swell) 600-700 km wide with an average height of about 965 m caused by the overthickened crust and thermal reheating of the oceanic lithosphere. The associated buoyancy flux corrected by the isostatic response of the overthickened crust is approximately 7.4 Mg/s.



3. The overriding plate is characterized by the presence of a lateral velocity gradient located 40–50 km landward of the trench where velocities jump from 5.0 to >6.0 km/s. This seismic feature is located beneath a prominent normal scarp of ~1.5 km of vertical offset and resembles the lithological contact between the eroded frontal part of the continental plate composed of volcanic and metamorphic rocks with the Paleozoic coastal block made of igneous rocks associated with the Arequipa Massif.
4. The normal bathymetric scarp observed in the ridge-trench collision zone is located in the shelf break and spatially coincides with a narrow continental slope of ~50 km wide and the seaward migration of the coastal line suggesting high uplift rates associated with the buoyant effect of the NR causing strong deformation of the upper plate.
5. The smooth and shallow seafloor topography of the NR is capable of generating relatively large thrust earthquakes such as the 1996 *Mw* 7.7 and 2011 *Mw* 6.9 events. However, the NR has behaved as a seismic barrier for along-strike rupture propagation of some megathrust earthquakes such as the 1746 *Mw* 8.6 and 1942 *Mw* 8.1 events.
6. Along dip, subduction erosion is more vigorous beneath the continental slope at low lithostatic pressures causing likely hydrofracturing and creeping aseismic behavior. In contrast, the 1996 and 2011 thrust earthquakes located beneath the shelf occurred along an interplate contact where subduction erosion is less intense and stick-slip behavior can occur.

#### Acknowledgments

We acknowledge the support of the Chilean National Science Foundation (FONDECYT) Grant 1170009 and the PIA/CONICYT Anillo de Investigación de Ciencia y Tecnología Grant ACT172002 project “The interplay between subduction processes and natural disasters.” J. R. acknowledges CONICYT for the support through FONDECYT project, Grant 1170804. We also acknowledge the constructive comments of Mark Richards, two anonymous reviewers, the Editor Taylor Schildgen, and Andrei Maksymowicz for providing the code GravGrad. The readers can access our seismic results at the following link ([https://osf.io/qftmk/?view\\_only=8d9f3d29c29b47a691c774c466dda5f5](https://osf.io/qftmk/?view_only=8d9f3d29c29b47a691c774c466dda5f5)).

#### References

- Adam, C., Vidal, V., & Bonneville, A. (2005). MiFil: A method to characterize seafloor swells with application to the south central Pacific. *Geochemistry, Geophysics, Geosystems*, 6, Q01003. <https://doi.org/10.1029/2004GC000814>
- Antoničević, S. K., Wagner, L. S., Kumar, A., Beck, S. L., Long, M. D., Zandt, G., et al. (2015). The role of ridges in the formation and longevity of flat slabs. *Nature*, 524(7564), 212–215. <https://doi.org/10.1038/nature14648>
- Atherton, M. P., & Aguirre, L. (1992). Thermal and geotectonic setting of Cretaceous volcanic rocks near Ica, Peru, in relation to Andean crustal thinning. *Journal of South American Earth Sciences*, 5(1), 47–69. [https://doi.org/10.1016/0895-9811\(92\)90059-8](https://doi.org/10.1016/0895-9811(92)90059-8)
- Ballance, P. F., Scholl, D. W., Vallier, T. L., Stevenson, A. J., Ryan, H., & Herzer, R. H. (1989). Subduction of a Late Cretaceous seamount of the Louisville Ridge at the Tonga Trench: A model of normal and accelerated tectonic erosion. *Tectonics*, 8(5), 953–962.
- Beck, S. L., & Ruff, L. J. (1989). Great earthquakes and subduction along the Peru trench. *Physics of the Earth and Planetary Interiors*, 57(3–4), 199–224. [https://doi.org/10.1016/0031-9201\(89\)90112-x](https://doi.org/10.1016/0031-9201(89)90112-x) ISSN 0031-9201
- Bello-González, J. P., Contreras-Reyes, E., & Arriagada, C. (2018). Predicted path for hotspot tracks off South America since Paleocene times: Tectonic implications of ridge-trench collision along the Andean margin. *Gondwana Research*, 64, 216–234. <https://doi.org/10.1016/j.gr.2018.07.008>
- Bilek, S. L. (2010). Invited review paper: Seismicity along the South American subduction zone: Review of large earthquakes, tsunamis, and subduction zone complexity. *Tectonophysics*, 495(1–2), 2–14. <https://doi.org/10.1016/j.tecto.2009.02.037>
- Boekhout, F., Sempere, T., Spikings, R., & Schaltegger, U. (2013). Late Paleozoic to Jurassic chronostratigraphy of coastal southern Peru: Temporal evolution of sedimentation along an active margin. *Journal of South American Earth Sciences*, 47, 179–200. <https://doi.org/10.1016/j.jsames.2013.07.003>
- Bourgeois, J., Pautot, G., Bandy, W., Boinet, T., Chotin, P., Huchon, P., et al. (1988). Seabeam and seismic reflection imaging of the tectonic regime of the Andean continental margin off Peru (4°S to 10°S). *Earth and Planetary Science Letters*, 87(1–2), 111–126. [https://doi.org/10.1016/0012-821X\(88\)90068-4](https://doi.org/10.1016/0012-821X(88)90068-4)
- Calmant, S., Francheteau, J., & Cazenave, A. (1990). Elastic layer thickening with age of the oceanic lithosphere: A tool for prediction of the age of volcanoes or oceanic crust. *Geophysical Journal International*, 100(1), 59–67. <https://doi.org/10.1111/j.1365-246X.1990.tb04567.x>
- Cande, S. C., & Haxby, W. F. (1991). Eocene propagating rifts in the southwest Pacific and their conjugate features on the Nazca plate. *Journal of Geophysical Research*, 96(B12), 19,609–19,622. <https://doi.org/10.1029/91JB01991>
- Charrier, R., Pinto, L., & Rodríguez, M. P. (2007). Tectonostratigraphic evolution of the Andean Orogen in Chile. In T. Moreno & W. Gibbons (Eds.), *The Geology of Chile* (pp. 21–114). London: The Geological Society. <https://doi.org/10.1144/GOCH.3>
- Clift, P., Pecher, I., Kukowski, N., & Hampel, A. (2003). Tectonic erosion of the Peruvian forearc, Lima Basin, by subduction and Nazca Ridge collision. *Tectonics*, 22(3), 1023. <https://doi.org/10.1029/2002TC001386>
- Cloos, M., & Shreve, R. L. (1996). Shear-zone thickness and the seismicity of Chilean- and Marianas-type subduction zones. *Geology*, 24(2), 107–110. [https://doi.org/10.1130/0091-7613\(1996\)024<0107:SZTATS>2.3.CO;2](https://doi.org/10.1130/0091-7613(1996)024<0107:SZTATS>2.3.CO;2)
- Contreras-Reyes, E., Becerra, J., Kopp, H., Reichert, C., & Díaz-Naveas, J. (2014). Seismic structure of the north-central Chilean convergent margin: Subduction erosion of a paleomagmatic arc. *Geophysical Research Letters*, 41, 1523–1529. <https://doi.org/10.1002/2013GL058729>
- Contreras-Reyes, E., & Carrizo, D. (2011). Control of high oceanic features and subduction channel on earthquake ruptures along the Chile-Peru subduction zone. *Physics of the Earth and Planetary Interiors*, 186(1–2), 49–58. <https://doi.org/10.1016/j.pepi.2011.03.002>
- Contreras-Reyes, E., Jara, J., Grevemeyer, I., Ruiz, S., & Carrizo, D. (2012). Abrupt change in the dip of the subducting plate beneath north Chile. *Nature Geoscience*, 5(5), 342–345. <https://doi.org/10.1038/ngeo1447>
- Cortés-Rivas, V., Contreras-Reyes, E., & Krabbenhoef, A. (2018). *Estructura y flexura de la dorsal de Nazca*. Concepción, Chile: XV Congreso Geológico Chileno.
- DeMets, C., Gordon, R. G., Argus, D. F., & Stein, S. (1990). Current plate motions. *Geophysical Journal International*, 101(2), 425–478. <https://doi.org/10.1111/j.1365-246X.1990.tb06579.x>
- Dominguez, S., Lallemand, S. E., Malavieille, J., & von Huene, R. (1998). Upper plate deformation associated with seamount subduction. *Tectonophysics*, 293(3–4), 207–224. [https://doi.org/10.1016/S0040-1951\(98\)00086-9](https://doi.org/10.1016/S0040-1951(98)00086-9)
- Dorbath, L., Cisternas, A., & Dorbath, C. (1990). Assessment of the size of large and great historical earthquakes in Peru. *Bulletin of the Seismological Society of America*, 80(3), 551–576.

- Dobrovine, P. V., Steinberger, B., & Torsvik, T. H. (2012). Absolute plate motions in a reference frame defined by moving hot spots in the Pacific, Atlantic, and Indian Oceans. *Journal of Geophysical Research*, *117*, B09101. <https://doi.org/10.1029/2011JB009072>
- Espurt, N., Funicello, F., Martinod, J., Guillaume, B., Regard, V., Faccenna, C., & Brusset, S. (2008). Flat subduction dynamics and deformation of the South American plate: Insights from analog modeling. *Tectonics*, *27*, TC3011. <https://doi.org/10.1029/2007TC002175>
- Grevenmeyer, I., Ranero, C. R., & Ivandic, M. (2018). Structure of oceanic crust and serpentinization at subduction trenches. *Geosphere*, *14*(2), 395–418. <https://doi.org/10.1130/GES01537.1>
- Gutscher, M. A., Spakman, W., Bijwaard, H., & Engdahl, E. R. (2000). Geodynamics of flat subduction: Seismicity and tomographic constraints from the Andean margin. *Tectonics*, *19*(5), 814–833. <https://doi.org/10.1029/1999TC001152>
- Hampel, A. (2002). The migration history of the Nazca Ridge along the Peruvian active margin: A re-evaluation. *Earth and Planetary Science Letters*, *203*(2), 665–679. [https://doi.org/10.1016/S0012-821X\(02\)00859-2](https://doi.org/10.1016/S0012-821X(02)00859-2)
- Hampel, A., Kukowski, N., Bialas, J., Huebscher, C., & Heinbockel, R. (2004). Ridge subduction at an erosive margin: The collision zone of the Nazca Ridge in southern Peru. *Journal of Geophysical Research - Solid Earth*, *109*, B02101. <https://doi.org/10.1029/2003JB002593>
- Handschumacher, D. W. (1976). Post-Eocene plate tectonics of the eastern Pacific. *The Geophysics of the Pacific Ocean Basin and its Margin*, *19*, 177–202. <https://doi.org/10.1029/GM019p0177>
- Hsu, J. T. (1992). Quaternary uplift of the Peruvian coast related to the subduction of the Nazca Ridge: 13.5 to 15.6 degrees south latitude. *Quaternary International*, *15–16*, 87–97.
- INGEMET (2016). Mapa geológico del Perú, Escala 1:1,000,000.
- Jaillard, E., Soler, P., Carlier, G., & Mourier, T. (1990). Geodynamic evolution of the northern and central Andes during early to middle Mesozoic times: A Tethyan model. *Journal of the Geological Society*, *147*(6), 1009–1022. <https://doi.org/10.1144/gsjgs.147.6.1009>
- Kikuchi, M., & Kanamori, H. (1991). Inversion of complex body waves—III. *Bulletin of the Seismological Society of America*, *81*(6), 2335–2350.
- Kim, Y., & Clayton, R. W. (2015). Seismic properties of the Nazca oceanic crust in southern Peruvian subduction system. *Earth and Planetary Science Letters*, *429*, 110–121. <https://doi.org/10.1016/j.epsl.2015.07.055>
- Kopp, H., Flueh, E. R., Papenberg, C., & Klaeschen, D. (2004). Seismic investigations of the O'Higgins Seamount Group and Juan Fernández Ridge: Aseismic ridge emplacement and lithosphere hydration. *Tectonics*, *23*, TC2009. <https://doi.org/10.1029/2003TC001590>
- Korenaga, J., Holbrook, W. S., Kent, G. M., Kelemen, P. B., Detrick, R. S., Larsen, H.-C., et al. (2000). Crustal structure the southeast Greenland margin from joint refraction and reflection seismic tomography. *Journal of Geophysical Research*, *105*(B9), 21,591–21,614. <https://doi.org/10.1029/2000JB900188>
- Krabbenhoft, A., Bialas, J., Kopp, H., Kukowski, N., & Hübscher, C. (2004). Crustal structure of the Peruvian continental margin from wide-angle seismic studies. *Geophysical Journal International*, *159*(2), 749–764. <https://doi.org/10.1111/j.1365-246X.2004.02425.x>
- Kukowski, N., Hampel, A., Hoth, S., & Bialas, J. (2008). Morphotectonic and morphometric analysis of the Nazca plate and the adjacent offshore Peruvian continental slope—Implications for submarine landscape evolution. *Marine Geology*, *254*(1-2), 107–120. <https://doi.org/10.1016/j.margeo.2008.05.017>
- Kumar, A., Wagner, L. S., Beck, S. L., Long, M. D., Zandt, G., Young, B., & Minaya, E. (2016). Seismicity and state of stress in the central and southern Peruvian flat slab. *Earth and Planetary Science Letters*, *441*, 71–80. <https://doi.org/10.1016/j.epsl.2016.02.023>
- Le Pichon, X. L., Henry, P., & Lallemand, S. (1993). Accretion and erosion in subduction zones: The role of fluids. *Annual Review of Earth and Planetary Sciences*, *21*(1), 307–331. <https://doi.org/10.1146/annurev.ea.21.050193.001515>
- Le Roux, J. P., Correa, C. T., & Alayza, F. (2000). Sedimentology of the Rimac-Chillón alluvial fan at Lima, Peru, as related to Plio-Pleistocene sea-level changes, glacial cycles and tectonics. *Journal of South American Earth Sciences*, *13*(6), 499–510. [https://doi.org/10.1016/S0895-9811\(00\)00044-4](https://doi.org/10.1016/S0895-9811(00)00044-4)
- Loewy, S. L., Connelly, J. N., & Dalziel, I. W. D. (2004). An orphaned basement block: The Arequipa-Antofalla Basement of the central Andean margin of South America. *Geological Society of America Bulletin*, *116*(1), 171–187. <https://doi.org/10.1130/B25226.1>
- Lonsdale, P. (2005). Creation of the Cocos and Nazca plates by fission of the Farallon plate. *Tectonophysics*, *404*(3-4), 237–264. <https://doi.org/10.1016/j.tecto.2005.05.011>
- Ma, Y., & Clayton, R. W. (2015). Flat slab deformation caused by interplate suction force. *Geophysical Research Letters*, *42*, 7064–7072. <https://doi.org/10.1002/2015GL065195>
- Maksymowicz, A., Ruiz, J., Vera, E., Contreras-Reyes, E., Ruiz, S., Arraigada, C., & Bascuñán, S. (2018). Heterogeneous structure of the Northern Chile marine forearc and its implications for megathrust earthquakes. *Geophysical Journal International*, *215*(2), 1080–1097. <https://doi.org/10.1093/gji/ggy325>
- Maksymowicz, A., Tréhu, A. M., Contreras-Reyes, E., & Ruiz, S. (2015). Density-depth model of the continental wedge at the maximum slip segment of the Maule Mw8.8 megathrust earthquake. *Earth and Planetary Science Letters*, *409*, 265–277. <https://doi.org/10.1016/j.epsl.2014.11.005>
- McNutt, M., & Bonneville, A. (2000). A shallow, chemical origin for the Marquesas Swell. *Geochemistry, Geophysics, Geosystems*, *1*, 1014. <https://doi.org/10.1029/1999GC000028>
- Mukasa, S. B., & Henry, D. J. (1990). The San Nicolas Batholith of coastal Peru: Early Paleozoic continental arc or continental rift magmatism. *Journal of the Geological Society of London*, *147*(1), 27–39. <https://doi.org/10.1144/gsjgs.147.1.0027>
- Müller, R. D., Seton, M., Zahirovic, S., Williams, S., Matthews, K., Wright, N., et al. (2016). Ocean basin evolution and global-scale plate reorganization events since Pangea breakup. *Annual Review of Earth and Planetary Sciences*, *44*(1), 107–138. <https://doi.org/10.1146/annurev-earth-060115-012211>
- Norabuena, E., Leffler-Griffin, L., Mao, A., Dixon, T., Stein, S., Sacks, I. S., et al. (1998). Space geodetic observations of Nazca-South America convergence across the central Andes. *Science*, *279*(5349), 358–362. <https://doi.org/10.1126/science.279.5349.358>
- Okal, E. A., Borrero, J. C., & Synolakis, C. E. (2006). Evaluation of tsunami risk from regional earthquakes at Pisco, Peru. *Bulletin of the Seismological Society of America*, *96*(5), 1634–1648.
- Okal, E. A., & Newman, A. V. (2001). Tsunami earthquakes: The quest for a regional signal. *Physics of the Earth and Planetary Interiors*, *124*(1-2), 45–70. [https://doi.org/10.1016/S0031-9201\(01\)00187-X](https://doi.org/10.1016/S0031-9201(01)00187-X)
- Orellana-Rovirosa, F., & Richards, M. (2017). Rough versus smooth topography along oceanic hotspot tracks: Observations and scaling analysis. *Geophysical Research Letters*, *44*, 4074–4081. <https://doi.org/10.1002/2016GL072008>
- Pardo-Casas, F., & Molnar, P. (1987). Relative motion of the Nazca (Farallon) and South American plates since Late Cretaceous time. *Tectonics*, *6*(3), 233–248. <https://doi.org/10.1029/TC006i003p0233>
- Phipps Morgan, J., & Morgan, W. J. (1995). Hot-spot melting generates both hotspot volcanism and a hotspot swell? *Journal of Geophysical Research*, *100*(B5), 8045–8062. <https://doi.org/10.1029/94JB02887>

- Quenardelle, S., & Ramos, V. A. (1999). The Ordovician Western Sierras Pampeanas Magmatic Belt: Record of Argentine Precordillera accretion. *Geological Society of America Special Papers*, 336, 63–86. <https://doi.org/10.1130/0-8137-2336-1.63>
- Ramos, V. A. (2008). The basement of the Central Andes: The Arequipa and related terranes. *Annual Review of Earth and Planetary Sciences*, 36(1), 289–324. <https://doi.org/10.1146/annurev.earth.36.031207.124304>
- Ranero, C. R., & von Huene, R. (2000). Subduction erosion along the Middle America convergent margin. *Nature*, 404(6779), 748–752. <https://doi.org/10.1038/35008046>
- Ray, J. S., Mahoney, J. J., Duncan, R. A., Ray, J., Wessel, P., & Naar, D. F. (2012). Chronology and geochemistry of lavas from the Nazca Ridge and Easter Seamount Chain: An ~30 Myr hotspot record. *Journal of Petrology*, 53(7), 1417–1448. <https://doi.org/10.1093/petrology/egs021>
- Richards, M., Contreras-Reyes, E., Lithgow-Bertelloni, C., Ghiorso, M., & Stixrude, L. (2013). Petrological interpretation of deep crustal intrusive bodies beneath oceanic hotspot provinces. *Geochemistry, Geophysics, Geosystems*, 14, 604–619. <https://doi.org/10.1029/2012GC004448>
- Romero, D., Valencia, K., Alarcón, P., Peña, D., & Ramos, V. A. (2013). The offshore basement of Perú: Evidence for different igneous and metamorphic domains in the forearc. *Journal of South American Earth Sciences*, 42, 47–60. <https://doi.org/10.1016/j.jsames.2012.11.003>
- Rosenbaum, G., Giles, D., Saxon, M., Betts, P. G., Weinberg, R. F., & Duboz, C. (2005). Subduction of the Nazca Ridge and the Inca Plateau: Insights into the formation of ore deposits in Peru. *Earth and Planetary Science Letters*, 239(1-2), 18–32. <https://doi.org/10.1016/j.epsl.2005.08.003>
- Ruiz, J. A., Contreras-Reyes, E., Ortega-Culaciati, F., & Manriquez, P. (2018). Rupture process of the April 24, 2017, Mw 6.9 Valparaíso earthquake from the joint inversion of teleseismic body waves and near-field data. *Physics of the Earth and Planetary Interiors*, 279, 1–14. <https://doi.org/10.1016/j.pepi.2018.03.007>
- Saillard, M., Hall, S., Audin, L., Farber, D., Regard, V., & Hérail, G. (2011). Andean coastal uplift and active tectonics in southern Peru: <sup>10</sup>Be surface exposure dating of differentially uplifted marine terrace sequences (San Juan de Marcona, ~15.4°S). *Geomorphology*, 128(3-4), 178–190. <https://doi.org/10.1016/j.geomorph.2011.01.004>
- Salichon, J., Delouis, B., Lundgren, P., Giardini, D., Costantini, M., & Rosen, P. (2003). Joint inversion of broadband teleseismic and interferometric synthetic aperture radar (InSAR) data for the slip history of the Mw=7.7, Nazca ridge (Peru) earthquake of 12 November 1996. *Journal of Geophysical Research*, 108(B2), 2085. <https://doi.org/10.1029/2001JB000913>
- Sallares, V., Charvis, P., Flueh, E. R., & Bialas, J. (2003). Seismic structure of Cocos and Malpelo Volcanic Ridges and implications for hot spot-ridge interaction. *Journal of Geophysical Research*, 108(B12), 2564. <https://doi.org/10.1029/2003JB002431>
- Sallares, V., & Ranero, C. (2005). Structure and tectonics of the erosional convergent margin off Antofagasta, north Chile (23°30'S). *Journal of Geophysical Research*, 110, B06101. <https://doi.org/10.1029/2004JB003418>
- Sandwell, D., Garcia, E., Soofi, K., Wessel, P., Chandler, M., & Smith, W. H. (2013). Toward 1-mGal accuracy in global marine gravity from CryoSat-2, Envisat, and Jason-1. *The Leading Edge*, 32(8), 892–899. <https://doi.org/10.1190/tle32080892.1>
- Sennson, J. L., & Beck, S. L. (1996). Historical 1942 Ecuador and 1942 Peru subduction earthquakes and earthquake cycles along Colombia-Ecuador and Peru subduction segments. *Pure and Applied Geophysics*, 146(1), 67–101. <https://doi.org/10.1007/BF00876670>
- Seton, M., Whittaker, J. M., Wessel, P., Müller, R. D., DeMets, C., Merkouriev, S., et al. (2014). Community infrastructure and repository for marine magnetic identifications. *Geochemistry, Geophysics, Geosystems*, 15, 1629–1641. <https://doi.org/10.1002/2013GC005176>
- Sladen, A., Tavera, H., Simons, M., Avouac, J. P., Konca, A. O., Perfettini, H., et al. (2010). Source model of the 2007 Mw 8.0 Pisco, Peru earthquake: Implications for seismogenic behavior of subduction megathrusts. *Journal of Geophysical Research*, 115, B02405. <https://doi.org/10.1029/2009JB006429>
- Sleep, N. H. (1990). Hotspots and mantle plumes: Some phenomenology. *Journal of Geophysical Research*, 95(B5), 6715–6736. <https://doi.org/10.1029/JB095iB05p06715>
- Spence, W., Mendoza, E., Engdahl, E. R., Choy, G. L., & Norabuena, E. (1999). Seismic subduction of the Nazca ridge as shown by the 1996–1997 Peru earthquakes. *Pure and Applied Geophysics*, 154, 753–776. [https://doi.org/10.1007/978-3-0348-8679-6\\_16](https://doi.org/10.1007/978-3-0348-8679-6_16)
- Spikings, R., Cochrane, R., Villagomez, D., Van der Lelij, R., Vallejo, C., Winkler, W., & Beate, B. (2015). The geological history of north-western South America: From Pangaea to the early collision of the Caribbean Large Igneous Province (290–75 Ma). *Gondwana Research*, 27(1), 95–139. <https://doi.org/10.1016/j.gr.2014.06.004>
- Spikings, R., Reitsma, M. J., Boekhout, F., Mišković, A., Ulianov, A., Chiaradia, M., et al. (2016). Characterization of Triassic Rifting in Peru and implications for the early disassembly of western Pangaea. *Gondwana Research*, 35, 124–143. <https://doi.org/10.1016/j.gr.2016.02.008>
- Stern, C. R. (2011). Subduction erosion: Rates, mechanisms, and its role in arc magmatism and the evolution of the continental crust and mantle. *Gondwana Research*, 20(2-3), 284–308. <https://doi.org/10.1016/j.gr.2011.03.006>
- Tajima, F., & Kikuchi, M. (1995). Tectonic implications of the seismic ruptures associated with the 1983 and 1991 Costa Rica earthquakes. In *Geologic and tectonic development of the Caribbean Plate boundary in southern Central America* (pp. 295–327). Washington, DC. <https://doi.org/10.1130/SPE295-p327>
- Troll, C. (1968). Geo-ecology of the mountainous regions of the tropical Americas. In *Geo-ecology of the mountainous regions of the tropical Americas* (pp. 223–236). Bonn.
- Turcotte, D., & Schubert, G. (2014). *Geodynamics*. Cambridge: Cambridge University Press. <https://doi.org/10.1017/CBO9780511843877>
- Van Rijsingen, E., Lallemand, S., Peyret, M., Arcay, D., Heuret, A., Funicello, F., & Corbi, F. (2018). How subduction interface roughness influences the occurrence of large interplate earthquakes. *Geochemistry, Geophysics, Geosystems*, 19(8), 2342–2370. <https://doi.org/10.1029/2018GC007618>
- Villegas, J. C., & Tavera, H. (2010). Modelo de estructura de velocidad cortical 1D para la región norte del Perú a partir de sismos locales. *Boletín de la Sociedad Geológica del Perú*, 104, 81–91.
- Villegas-Lanza, J. C., Chlieh, M., Cavalié, O., Tavera, H., Baby, P., Chire-Chira, J., & Nocquet, J.-M. (2016). Active tectonics of Peru: Heterogeneous interseismic coupling along the Nazca megathrust, rigid motion of the Peruvian Sliver, and Subandean shortening accommodation. *Journal of Geophysical Research: Solid Earth*, 121, 7371–7394. <https://doi.org/10.1002/2016JB013080>
- von Huene, R., Pecher, I. A., & Gutscher, M. A. (1996). Development of the accretionary prism along Peru and material flux after subduction of Nazca Ridge. *Tectonics*, 15(1), 19–33. <https://doi.org/10.1029/95TC02618>
- Wang, K., & Bilek, S. L. (2011). Do subducting seamounts generate or stop large earthquakes? *Geology*, 39(9), 819–822. <https://doi.org/10.1130/G31856.1>
- Watts, A. B. (2001). *Isostasy and flexure of the lithosphere*. Cambridge: Cambridge University Press.

- Watts, A. B., Koppers, A. A., & Robinson, D. P. (2010). Seamount subduction and earthquakes. *Oceanography*, 23(01), 166–173. <https://doi.org/10.5670/oceanog.2010.68>
- Wipf, M., Zeilinger, G., Seward, D., & Schlunegger, F. (2008). Focused subaerial erosion during ridge subduction: Impact on the geomorphology in south-central Peru. *Terra Nova*, 20(1), 1–10. <https://doi.org/10.1111/j.1365-3121.2007.00780.x>
- Woods, T. M., & Okal, E. A. (1994). The structure of the Nazca Ridge and the Sala y Gomez seamount chain from dispersion of Rayleigh waves. *Geophysical Journal International*, 117(1), 205–222. <https://doi.org/10.1111/j.1365-246X.1994.tb03313.x>
- Zelt, C. A., & Smith, R. B. (1992). Seismic traveltimes inversion for 2-D crustal velocity structure. *Geophysical Journal International*, 108(1), 16–34. <https://doi.org/10.1111/j.1365-246X.1992.tb00836.x>
- Zeumann, S., & Hampel, A. (2015). Deformation of erosive and accretive forearcs during subduction of migrating and non-migrating aseismic ridges: Results from 3-D finite element models and application to the Central American, Peruvian, and Ryukyu margins. *Tectonics*, 34, 1769–1791. <https://doi.org/10.1002/2015TC003867>